Research in Astronomy and Astrophysics, 25:065003 (13pp), 2025 June

https://doi.org/10.1088/1674-4527/adcefe
CSTR: 32081.14.RAA.adcefe

An Analysis of the Seeing Conditions at Platform C of the Lenghu Site

Tian Lan[1,2,3], Licai Deng[2,3,4], Taoran Li[2,3], Fan Yang[2,3], Fei He[4,5], Chunguang Zhang[2], Kun Wang[5], Chen Yang[2,4], Ruiyue Li[2,3], and Tianlu Chen[1]

[1] Department of Physics, College of Science, Xizang University, Lhasa 850000, China; lantian@bao.ac.cn
[2] Key Laboratory of Optical Astronomy, National Astronomical Observatories, Chinese Academy of Sciences, Beijing 100101, China; licai@bao.ac.cn
[3] School of Astronomy and Space Science, University of Chinese Academy of Sciences, Beijing 100049, China
[4] Institute of Geology and Geophysics, Chinese Academy of Sciences, Beijing 100029, China
[5] School of Physics and Astronomy, China West Normal University, Nanchong 637009, China
Received 2025 March 13; revised 2025 April 7; accepted 2025 April 9; published 2025 May 27

Abstract

This paper statistically analyzes the seeing data at the Lenghu site Platform C from 2018 to 2024, during which extensive construction modified the original landscape. The study focuses on the impacts of meteorological factors and building obstructions. The results reveal a progressive degradation in seeing as the monitoring setup passively changed: the median values were 0.″76 (the original location), 0.″83 during the Terrace, and 0.″99 at the new Dome (temporarily considered the permanent monitoring location). Once the instruments are fully deployed, wind speed and wind direction critically affect seeing quality, with optimal conditions occurring when the wind speed is 2–6 m s^{-1} and the wind direction is between 180° and 270°. However, in 2023 and 2024, the wind speeds decreased, and the prevailing wind direction shifted from southwest to northwest, correlating with poorer seeing. Computational Fluid Dynamics simulations reveal that the construction of the Wide Field Survey Telescope altered the local wind field, increasing turbulence around the Dome, especially when the winds blow from 225° to 255°. In contrast, Platform A, located in a higher and more open area, consistently maintained better seeing, particularly after midnight, likely due to fewer obstructions and lower nocturnal heat release.

Key words: site testing – methods: statistical – hydrodynamics – atmospheric effects

1. Introduction

Astronomical seeing refers to the distortion of the radiation wave front from cosmic sources, caused by fluctuations in the refractive index of the air (Giovanelli et al. 2001). It directly impacts the quality of astronomical images and the resolution of spatial objects observed. Therefore, it is a key parameter in site selection and the performance of ground-based telescopes (Tokovinin 2023).

Since 1985, numerous international research teams have performed site evaluations for prestigious observatories. These evaluations include Mount Locke in Texas, USA (Barker 1987); La Silla and Paranal in Chile (Woltjer 1991); Maunakea in Hawaii, USA (Bely 1987); and Roque de los Muchachos in La Palma, Spain (Munoz-Tunon et al. 1997). These evaluations play a vital role in determining suitable locations for astronomical observatories, as optimal seeing conditions are necessary for high-quality observations. For example, the La Silla Observatory in Chile systematically records astronomical seeing data through a fully automated Differential Image Motion Monitor (DIMM) and publishes monthly averages on the European Southern Observatory (ESO) website (https://www.eso.com). This continuous monitoring provides invaluable data for both site assessment and ongoing scientific observations. Similarly, Van Kooten & Izett (2022) evaluated the seeing conditions at Maunakea over the past 40 yr utilizing data from a MASS-DIMM system, concluding that these conditions have remained relatively stable, which is essential for future astronomical observations. Likewise, Liu et al. (2015) analyzed the seeing conditions at the Xinglong station in China from 1995 to 2001, documenting a range of 2″–5″ and revealing notable seasonal variations. Furthermore, Feng et al. (2020) assessed seeing data from the Ali, Muztagh, and Daocheng sites from 2017 March to 2019 March, reporting values of 1.″17, 0.″90 and 1.″01, respectively, in conjunction with other meteorological parameters. The analysis provided support for the selection of a 12 m optical/infrared telescope for placement in western China. Lastly, Deng et al. (2021) investigated the seeing conditions at the Saishiteng Mountain site in Lenghu, China, from 2018 October to 2020 December. They reported a median seeing of 0.″75, which indicates the site's potential for future scientific research.

In summary, an excellent astronomical observatory should have extremely high requirements for seeing conditions. These conditions improve the operational efficiency of telescopes and the attached scientific instruments on the site, thereby enhancing the precision and reliability of the data collected and the scientific results. As a standard procedure for an astronomical observatory, ongoing monitoring of atmospheric

Figure 1. Panoramic view of point C. In the figure, 1, 2, and 3 correspond to the phases in Table 1.

and meteorological parameters, especially seeing, provides essential support and valuable data for advancing future astronomical research.

Seeing represents the distribution and intensity of atmospheric turbulence, including properties of the ground surface layer, the boundary layer, and the free atmosphere (Giovanelli et al. 2001). Among those, near-surface turbulence is an important factor influencing seeing variations, closely related to ground-level wind shear and temperature gradients. Near-surface turbulence is also affected by local topography, vegetation, and buildings, which exhibit strong locality (Coulman 1985). Specifically, changes in topography alter local wind fields, while buildings and vegetation impact seeing by generating eddies and airflow disturbances through localized heating or shading of the wind flow. In addition, atmospheric parameters such as temperature, relative humidity, and precipitable water vapor have an effect on seeing conditions (Jabiri et al. 2000). Human activities and ground conditions, such as roads and buildings, intensify near-surface turbulence by modifying local heat fluxes and temperature gradients, as well as altering the wind flow patterns (Blocken & Carmeliet 2004). Collectively, these factors contribute to variations in seeing, which in turn affect the quality of astronomical observations.

Recent statistical analysis of the seeing data from Platform C in Lenghu revealed a degradation in seeing quality, with the landscape being gradually modified, and the location of our equipment also changed. This study aims to analyze the factors that affect seeing variations, focusing on wind speed, wind direction, and building placement, to determine whether the DIMM should be relocated.

The Lenghu site has several mountain ridges that finally converge at a local summit of about 4500 m in altitude. Following preliminary construction (the top: blasted and flattened), three major platforms were made for telescope projects, namely Platform A (4304 m), Platform B (4300 m), and Platform C (4200 m). Most of the site quality measurements were collected at Platform C, while some site data were taken also at Platform A in the first half of 2024.

Table 1
Location of the DIMM During Different Periods

Phase	Location	Time
C1	Original location	2018.10.28–2020.08.31
C2	Terrace	2020.09.01–2023.01.31
C3	Dome	2023.02.01–2024.06.24

The layout of this paper is as follows: Section 2 introduces the underlying principles of the DIMM technique, the method for processing seeing data, and preliminary results. In Section 3, we provide a detailed analysis of the factors affecting seeing, such as wind speed, wind direction, and building obstructions. Section 4 compares the seeing data from Platform A and Platform C from mid-March to early 2024 June, highlighting differences in seeing trends before and after midnight and the influence of local microclimatic effects on seeing conditions. Section 5 examines the seasonal characteristics of seeing quality from 2022 to 2024, with a focus on wind direction patterns and their impact on seeing performance, particularly for Platform C. Finally, Section 6 summarizes the main conclusions and provides recommendations for future work.

2. Seeing Data Analysis

2.1. Observation Site and Instrumentation

The Lenghu site is located at the summit of Saishiteng Mountain, east of the Altun Mountains and on the northern edge

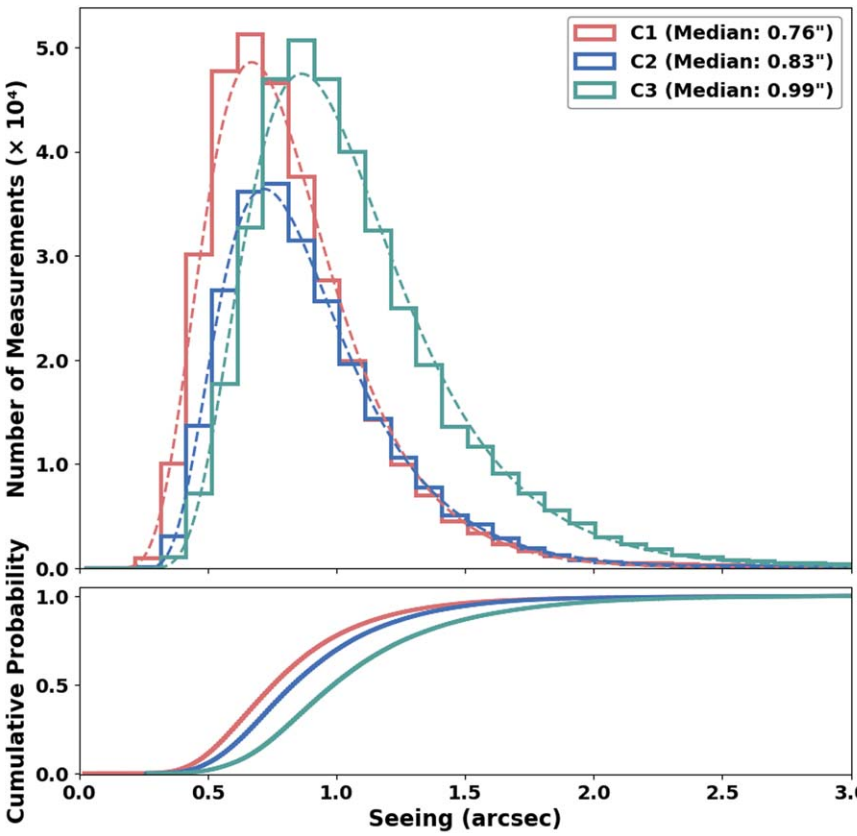

Figure 2. The figure above presents the seeing histograms for the three locations, including the median seeing values. The three dashed lines in the figure fit the histogram with a log-normal distribution. The lower figure illustrates the cumulative distribution.

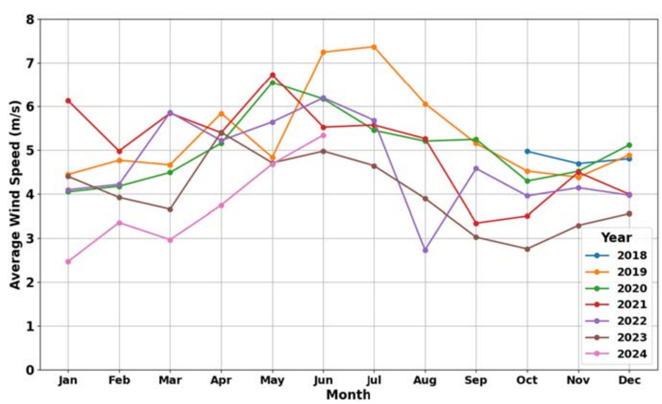

Figure 3. The monthly average wind speed for each year from 2018 October to 2024 June.

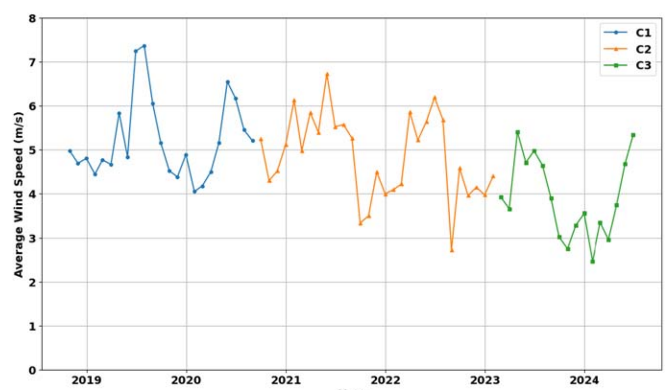

Figure 4. Temporal variation of monthly average wind speed (2018–2024) across different observation phases based on three phases.

Table 2
Percentiles of Seeing for the Three Locations (arcsec)

	10%	25%	50%	75%	95%
C1	0.49	0.60	0.76	0.97	1.44
C2	0.55	0.67	0.83	1.06	1.53
C3	0.66	0.80	0.99	1.26	1.86

of the Qaidam Basin. Six years of continuous monitoring data demonstrate Lenghu's exceptionally favorable climate for astronomical observations. Specifically, 70% of the nights throughout the year are clear and suitable for photometry, with a median seeing of $0''.75$. Nighttime temperature variations are minimal, averaging 2.4°C. Additionally, 55% of the nights exhibit

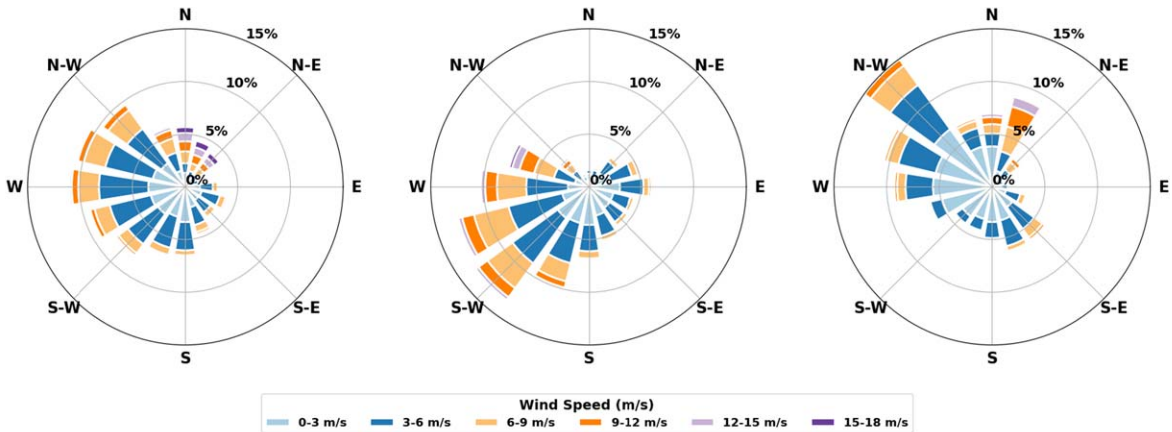

Figure 5. The wind rose frequency by three locations from 2018 October to 2024 June. From left to right are C1, C2, and C3 respectively.

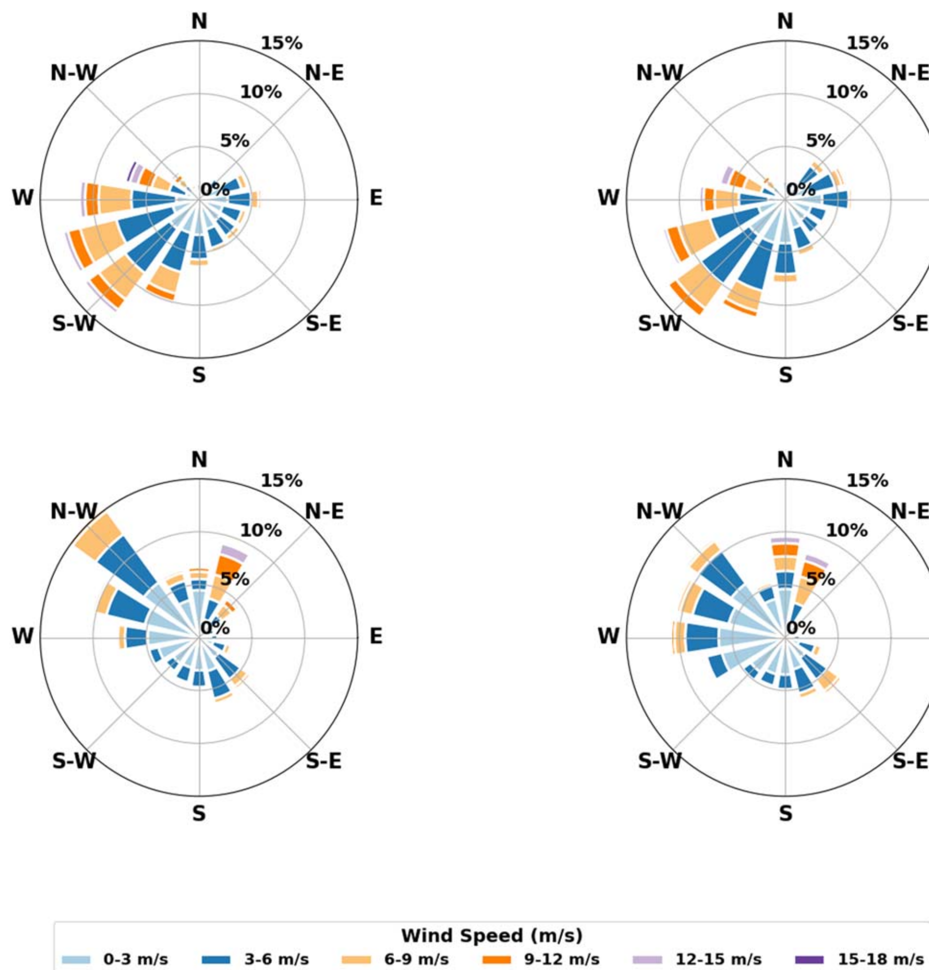

Figure 6. The frequency of wind roses from 2021 to 2024 by year, with subplots arranged as: top-left (2021), top-right (2022), bottom-left (2023), and bottom-right (2024).

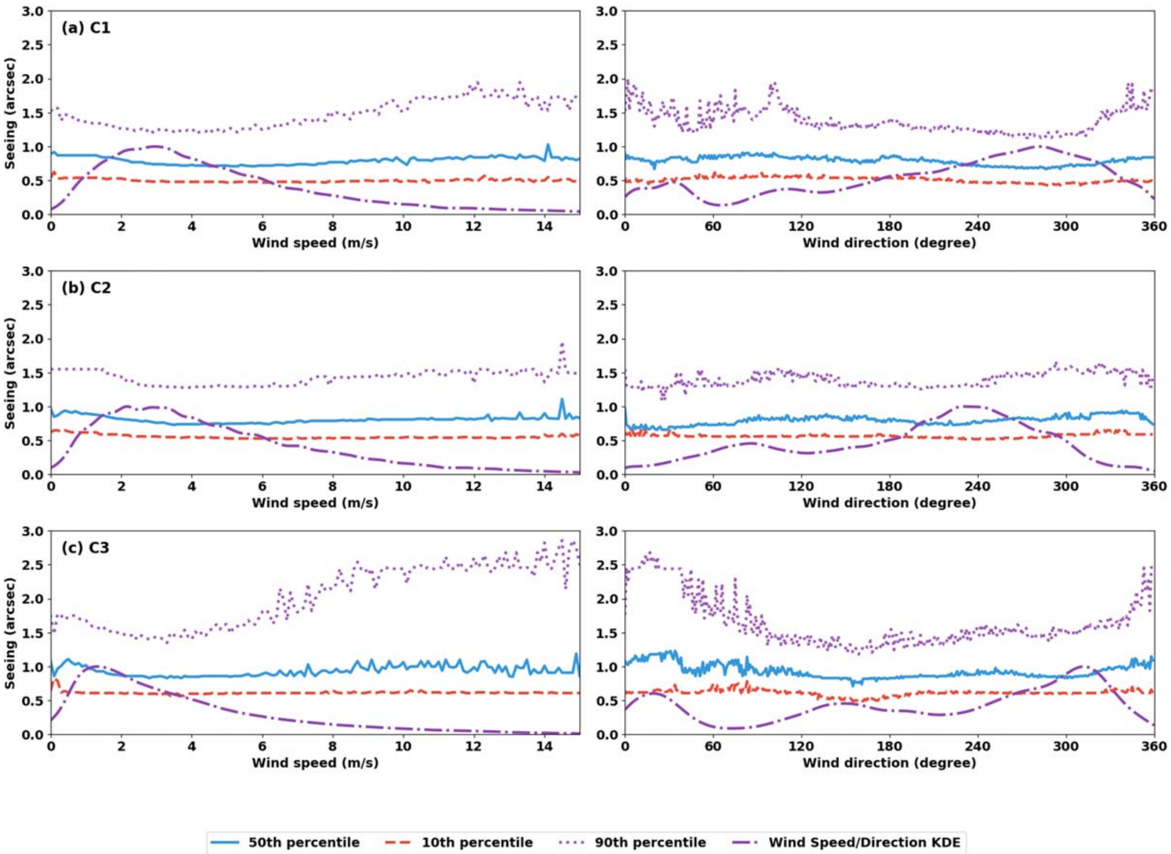

Figure 7. Panels (a), (b), and (c) correspond to C1, C2, and C3, respectively. The left column illustrates the variation of seeing with wind speed, while the right column shows its variation with wind direction.

Table 3
The Proportion of Wind Direction (195°–360°) at Three Different Locations

Location	195°	210°	225°	240°	255°	270°	285°	300°	315°	330°	345°	360°
C1	3.10	3.49	4.58	5.23	6.07	6.94	7.62	6.40	5.89	5.81	4.51	6.19
C2	5.41	7.37	9.80	10.45	9.54	8.44	7.94	6.99	2.82	1.41	1.09	0.53
C3	2.18	1.54	1.63	1.96	3.02	5.32	5.53	8.27	11.41	6.51	2.38	4.27

precipitable water vapor levels below 2 mm. The night sky is exceptionally dark, with almost no light pollution (Deng et al. 2021). These conditions underscore Lenghu's potential as a premier astronomical site. The Lenghu site hosts several observation platforms. Platform C, the first to be constructed, has an altitude of 4200 m, where the aforementioned parameters are monitored. Platform A, with an altitude of 4304 m, has a meteorological station that was established this year to monitor environmental parameters. The straight-line distance between these two platforms is approximately 1 km. This paper focuses on the data and environmental conditions at Platform C, with the conditions measured at Platform A included for reference. Figure 1 presents a panoramic view of Platform C, and Table 1 shows the DIMM device that was positioned at different locations during three distinct observation periods. The three phases mentioned below are consistent with those in Table 1. The DIMM was initially installed at the Original location (hereafter referred to as C1) in 2018 October, when the surroundings were open and unobstructed. Due to subsequent construction activities, the DIMM was relocated to the Terrace (C2). In 2023 February, with new construction planned around the Terrace area, the DIMM was moved once again to its current location (C3). The Dome containing the DIMM was mounted on a tower of 10 m in height; the locations are marked by numbers in Figure 1.

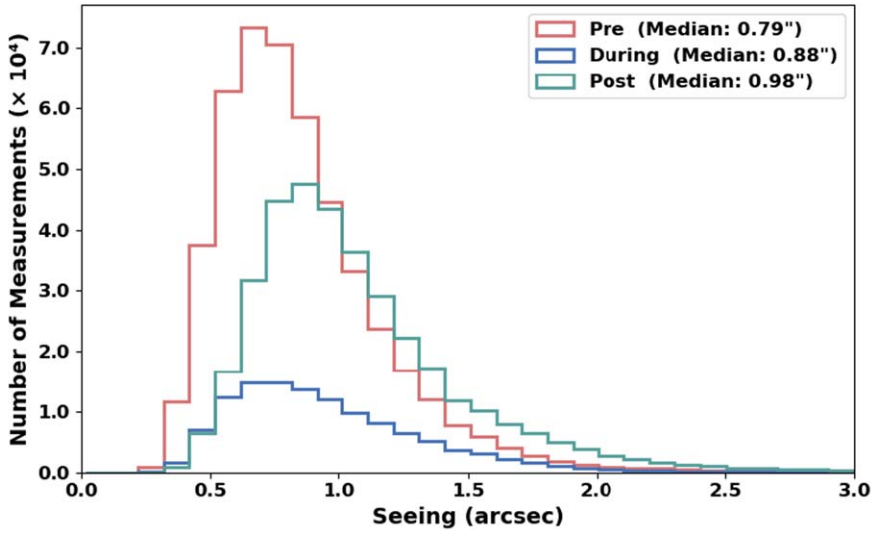

Figure 8. Histogram of seeing measurements from 2018 to 2024. The red, blue, and green lines represent the pre-construction (2018 October–2021 May), during-construction (2021 June–2023 July), and post-construction (2023 August–2024 June) phases, respectively.

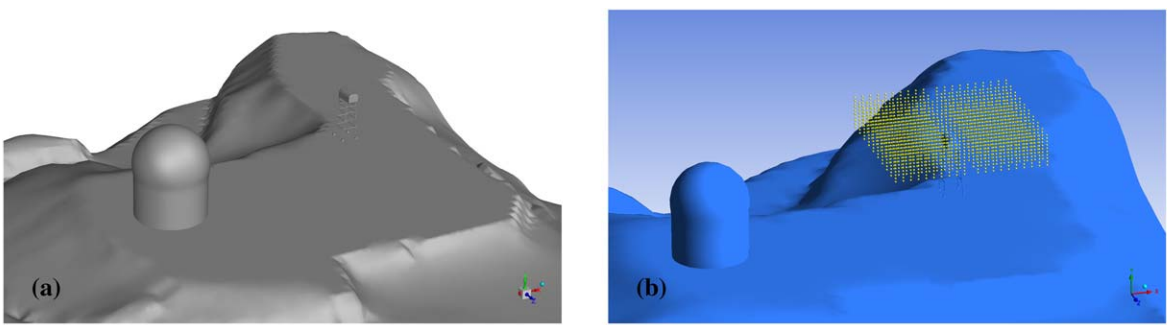

Figure 9. (a) 3D wind environment model, terrain, and telescope geometry. (b) Schematic of 2000 sampling points.

Seeing refers to the degradation of image quality in ground-based telescope observations due to atmospheric turbulence, which results in image blurring. The full width at half maximum of the point-spread function of a point source (star) quantifies seeing and expresses it in angular units (arcseconds or radians). This reflects the integrated atmospheric turbulence along the entire light path, characterized by the refractive index structure constant (Roddier 1981; Tokovinin 2023). Seeing measurements using DIMMs have been widely used in several site-selection campaigns and have become a standard assessment of integrated atmospheric optical turbulence (Zhu et al. 2023). This study employs a standard French DIMM device from Alcor-System, which measures the wave front slope differences between two pupils on a shared telescope mount, as described in Sarazin & Roddier (1990). Additionally, we calculated these measurements at the average wavelength of 550 nm and corrected them to the zenith position (airmass unity).

2.2. Data Preprocessing

A total of 1,125,467 seeing records were collected between 2018 October 28 and 2024 June 24. To ensure data quality, the records were cross-matched with system-recorded clear weather conditions (sky = 1) and outliers with seeing values above 3″ were excluded, as such values typically indicate poor observation conditions irrelevant for high-precision analysis. A rolling window of 10 data points was applied, using rolling averages and standard deviations to filter the data. A threshold of 1.5 standard deviations was selected based on a detailed analysis, including testing multiple thresholds and validating against data continuity, ensuring that it accurately identifies outliers without excluding valid data points. Seeing values exceeding this threshold were marked as outliers, and discontinuities were flagged where differences between consecutive data exceeded 0.5 arcsec, 0$''$.5, indicating potential anomalies. Further filtration retained only data collected during the astronomical twilight and dawn periods for improved accuracy. Given the inconsistent intervals in data recording, time-weighting was applied using an exponential decay function with a time constant of approximately 20 s. The weight calculation formula is

$$\text{weight} = \exp\left(-\frac{\Delta t}{\tau}\right),$$

where Δt is the time difference between adjacent data, and τ is the time constant. We normalized the weights to ensure the total weight summed to 1. Furthermore, we excluded data with intervals over 300 s to minimize the impact of irregular or anomalous time intervals on the final analysis. The weighting process had a minimal impact on the observed percentiles, affecting them by only 0$''$.01. Data analysis, based on different DIMM locations, indicates a gradual deterioration in seeing quality across observation phases. The median seeing values for C1, C2, and C3 were 0$''$.76, 0$''$.83, and 0$''$.99, respectively (see Figure 2 and Table 2). The cumulative distribution and percentile analyses further support this observation, with larger seeing values (indicating worse conditions) becoming more frequent during C3, underscoring its negative impact on seeing conditions.

3. A Comprehensive Analysis of Seeing Variability Factors

3.1. Wind Speed and Wind Direction

We processed wind speed data collected between 2018 and 2024, focusing on observations from the astronomical twilight and dawn. We aggregated the data monthly to capture variations in wind speed during key observation periods. To explore the location-specific wind speed characteristics, we categorized the monthly average wind speeds by the three locations. As shown in Figure 3, overall wind speeds in 2023 and 2024 were lower than in previous years. Figure 4 presents the monthly average wind speeds across each location, showing consistently lower speeds during C3. For safety and data quality, the remote-controlled DIMM dome opens only when wind speeds remain below 10 m s^{-1}. If wind speeds exceed 12 m s^{-1} for 3 minutes or reach 15 m s^{-1} for 1 minute, the system suspends observations.

In the wind direction analysis, we created wind rose charts for Platform C, dividing the wind direction data into three locations (see Figure 5) and displaying the annual distributions from 2021 to 2024 (see Figure 6). Meanwhile, we also present the proportions of wind directions ranging from 195° to 360° (in 15° intervals) for the three different locations, as shown in Table 3. The analysis results indicate a shift in the dominant wind direction from southwest to northwest, along with an increase in north winds. This could be attributed to the differences in terrain slope at the three locations, leading to changes in local wind flow patterns. In addition, we speculate that C3 may also be affected by the Wide Field Survey Telescope (WFST) obstruction. Further analysis of wind speed, wind direction, and seeing conditions reveals that optimal seeing occurs at wind speeds between 2 and 6 m s^{-1} and wind directions from 180° to 270° (see Figure 7).

Table 4
Median Turbulence (%) Results for All Sampling Points at Different Wind Directions

Wind Direction	WFST+C3 (%)	C3 (%)
15°	0.70	0.69
30°	0.85	0.84
45°	0.52	0.49
60°	0.46	0.45
75°	0.46	0.45
90°	0.47	0.46
105°	0.50	0.50
120°	0.52	0.52
135°	0.55	0.53
150°	0.68	0.66
165°	0.50	0.49
180°	0.44	0.42
195°	0.50	0.50
210°	0.56	0.65
225°	2.70	2.49
240°	2.89	1.29
255°	1.78	0.98
270°	0.91	0.95
285°	0.85	0.98
300°	1.61	1.70
315°	2.30	2.29
330°	0.81	0.88
345°	0.72	0.74
360°	0.71	0.71

3.2. Building Obstruction

For ground-based observatories, airflow interference between buildings impacts both the microclimate and seeing conditions. When the wind strikes the windward surface of a building, it disrupts the local wind fields and alters the microclimate. As airflow bypasses the building, strong vortices form on the leeward side. These vortices gradually weaken as they extend along the downwind direction, with the wake region typically reaching five to six times the building height. Consequently, these airflow disturbances modify the wind environment surrounding the telescope, increasing air turbulence and ultimately deteriorating the seeing conditions (Li & Jiang 2022).

The WFST has a height of 21 m and a dome diameter of 17.1 m. It is located approximately 19° west-southwest (WSW)

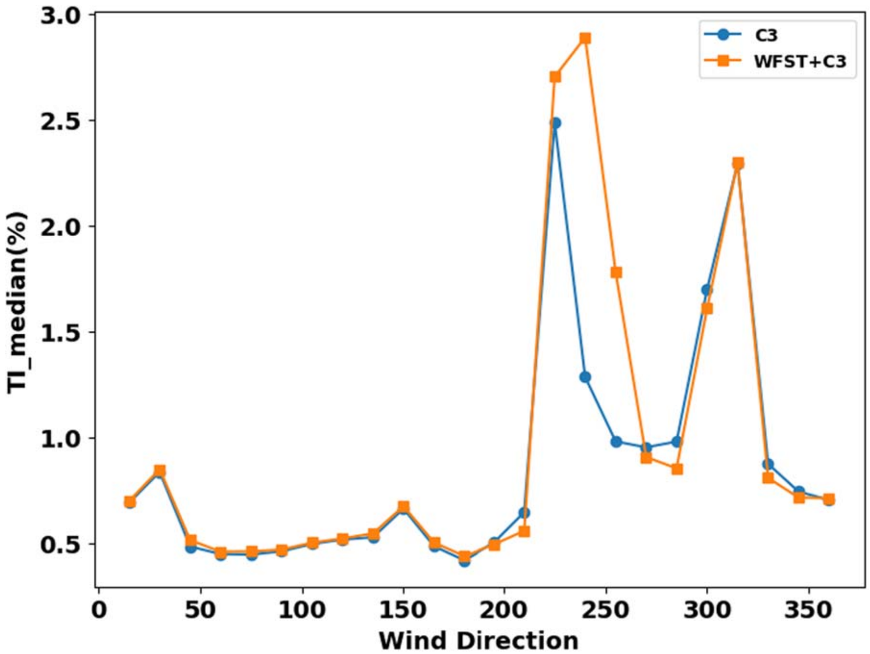

Figure 10. Turbulence intensity curves for all sampling points.

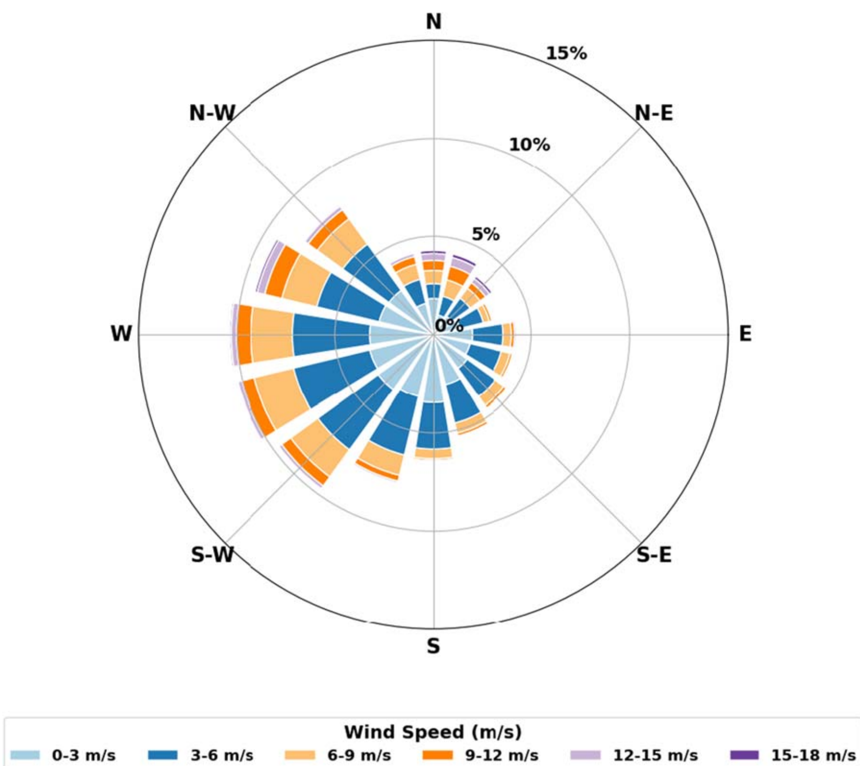

Figure 11. The wind rose diagrams from 2018 October to 2024 June.

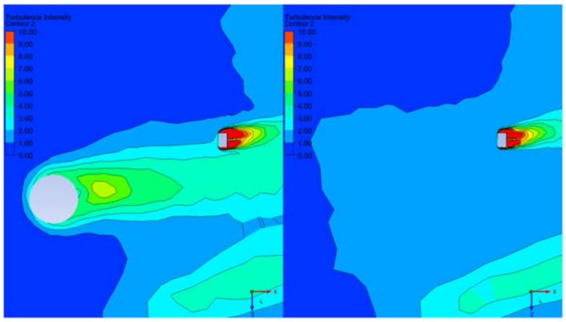

(a) 225°

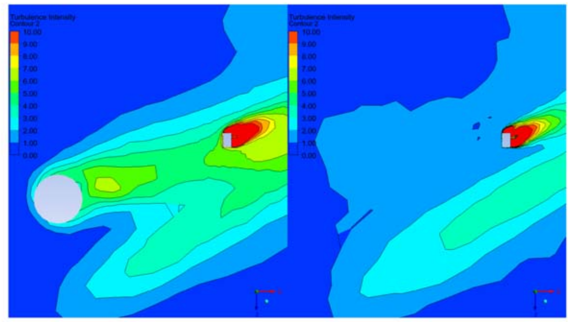

(b) 240°

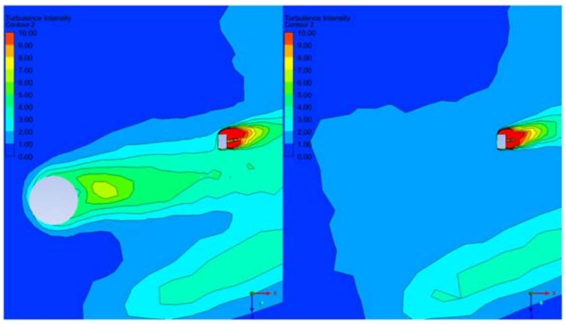

(c) 251°

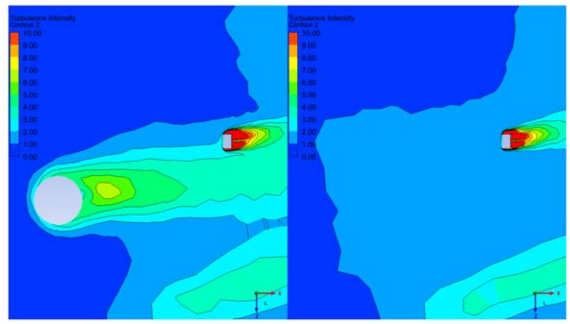

(d) 255°

Figure 12. Contours of turbulence intensity comparison plots with and without WFST under different prevailing wind directions (top view), where the gray circular and rectangular objects represent the WFST and C3, respectively. In panel (c), the prevailing wind direction of 251° corresponds to a line connecting the WFST and C3.

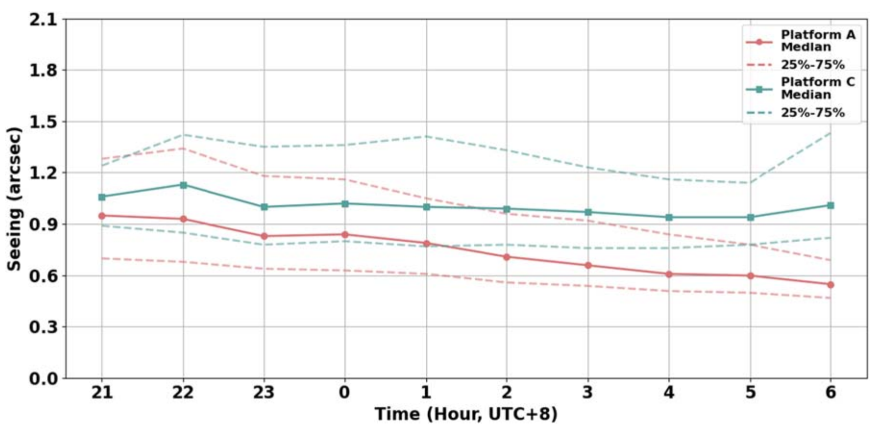

Figure 13. The temporal trends in seeing at Platform A and Platform C. The three lines, ordered from top to bottom, represent the 75th, 50th, and 25th percentiles, respectively. The red line corresponds to Platform A, while the green line represents Platform C. Evidently, the seeing at Platform A consistently surpasses that at Platform C.

of C3, at a distance of about 61 m. Construction began in 2021 May and ended in 2023 July. To assess the WFST's impact on seeing conditions, we categorized seeing data from 2018 to 2024 into three phases: pre-construction (2018 October–2021 May), during construction (2021 June–2023 July), and post-construction (2023 August–2024 June).

Statistical analysis revealed median seeing values of $0\farcs79$, $0\farcs88$, and $0\farcs98$ for these phases (in Figure 8). It should be noted that the variations in seeing values across different phases in Figure 8 are primarily influenced by the local topography. Natural variations in the atmospheric conditions may also contribute to these discrepancies. Due to the WFST's

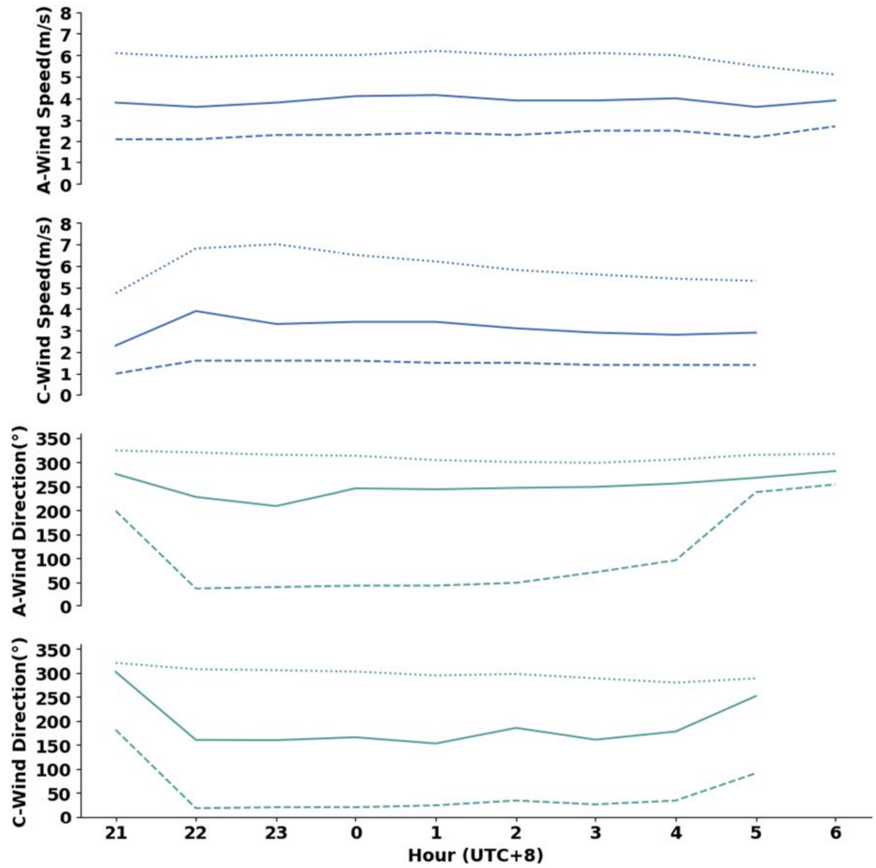

Figure 14. The temporal variations of wind speed and wind direction for Platform A and Platform C. Wind direction is represented by green lines and wind speed by blue lines. For each parameter, three lines correspond to the 75th, 50th, and 25th percentiles, ordered from top to bottom respectively.

height and its position, C3 lies within the WFST downwind wake disturbance area. These disturbances may alter the local wind field and microclimate, adversely affecting seeing conditions. Of course, the decline in seeing cannot be excluded as being influenced by topographical factors and changes in natural conditions. We built a three-dimensional (3D) model of the summit topology and the WFST (in Figure 9(a)) and performed several Computational Fluid Dynamics (CFD) simulations to study the wind environment of Platform C. In the current analysis, we chose the pressure-based solver for momentum equations and the k-omega Shear Stress Transport model for turbulence without the energy equation. The inlet velocity is equal to an average wind speed of $4\,\mathrm{m\,s^{-1}}$, with wind directions ranging from 0° to 360° at intervals of 15°.

To collect turbulence intensity data for the cases with and without the WFST, 2000 sampling points were distributed around C3 (in Figure 9(b)). The median turbulence intensities are presented in Table 4, while the corresponding scatter plots are shown in Figure 10.

The results revealed differences in turbulence intensity between wind directions of 225°–255°. This is consistent with the prevailing west and southwest winds observed in the wind rose diagram for the period 2018–2024 (in Figure 11), and corresponds to the location of the WFST relative to C3. To further clarify, we also present turbulence intensity plots around C3 with and without the WFST for the prevailing wind directions at 225°, 240°, 251°, and 255°, as shown in Figure 12. These results suggest that the wind environment around C3 is influenced by the WFST. It is worth noting that the turbulence intensity discussed in this article refers solely to mechanical turbulence. Although it does not directly intensify optical turbulence, the chaotic redistribution of energy involved in this process can create more favorable conditions for thermal turbulence, thereby indirectly degrading astronomical seeing.

4. A Comparison with Platform A

The data from mid-March to early 2024 June were analyzed to compare the seeing between Platform A and Platform C. Platform A, approximately 100 m higher than Platform C, is in an open area without obstructions. The time series presented in Figure 13 shows that while the trends on both platforms are similar before midnight, Platform A consistently outperforms

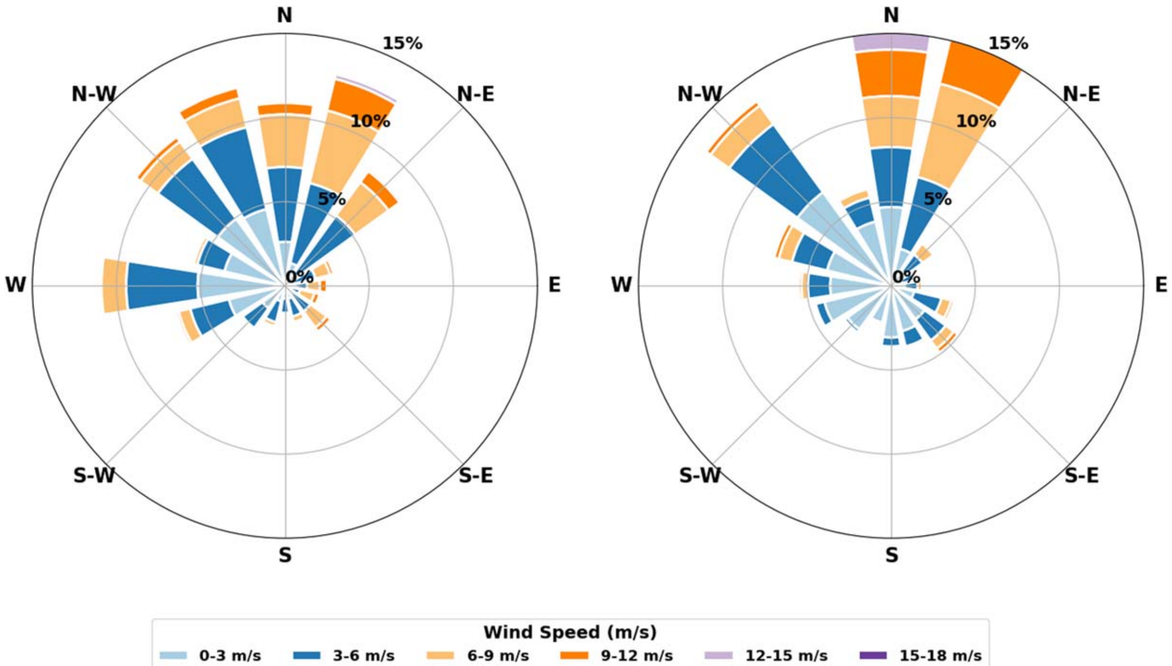

Figure 15. Wind rose diagrams for Platform A (left) and Platform C (right), covering the period from 2024 March to June.

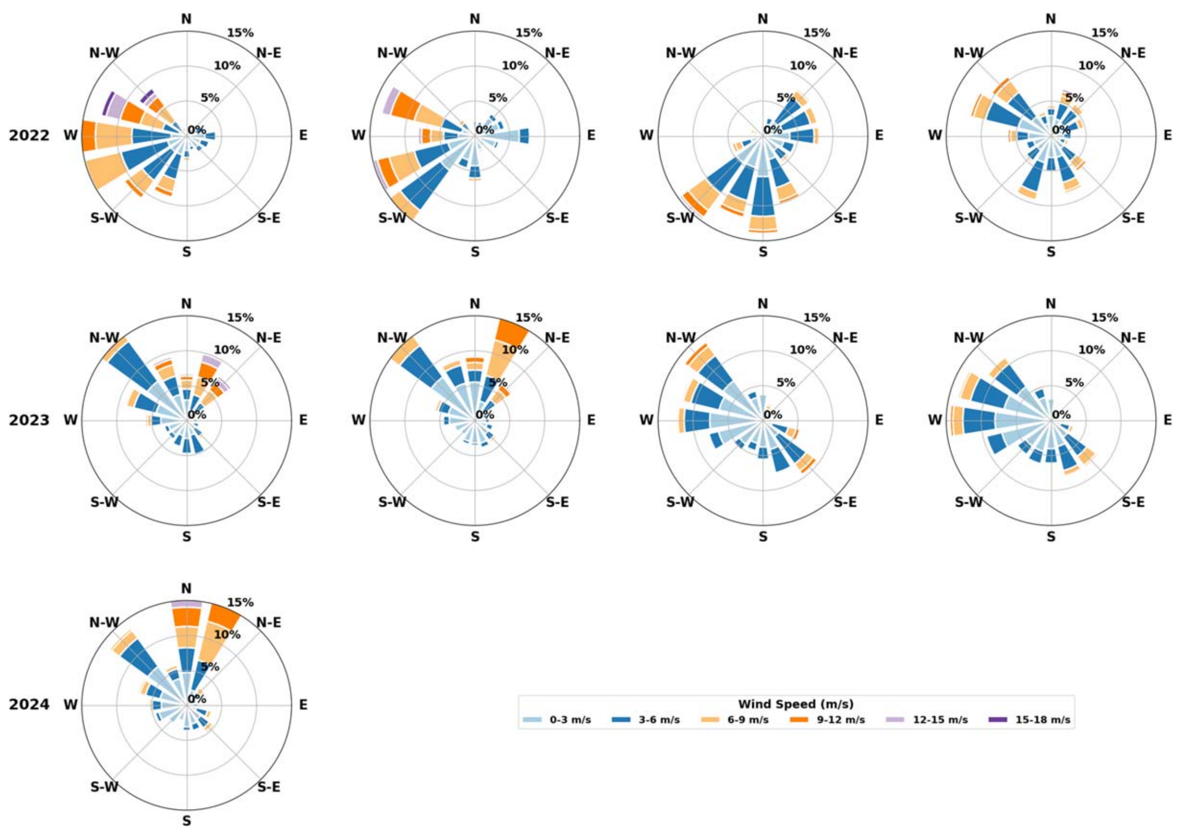

Figure 16. The wind rose and seeing statistics for Platform C from 2022 to 2024, organized into three rows (from top to bottom) for the years and four columns (from left to right) for spring, summer, fall, and winter, respectively.

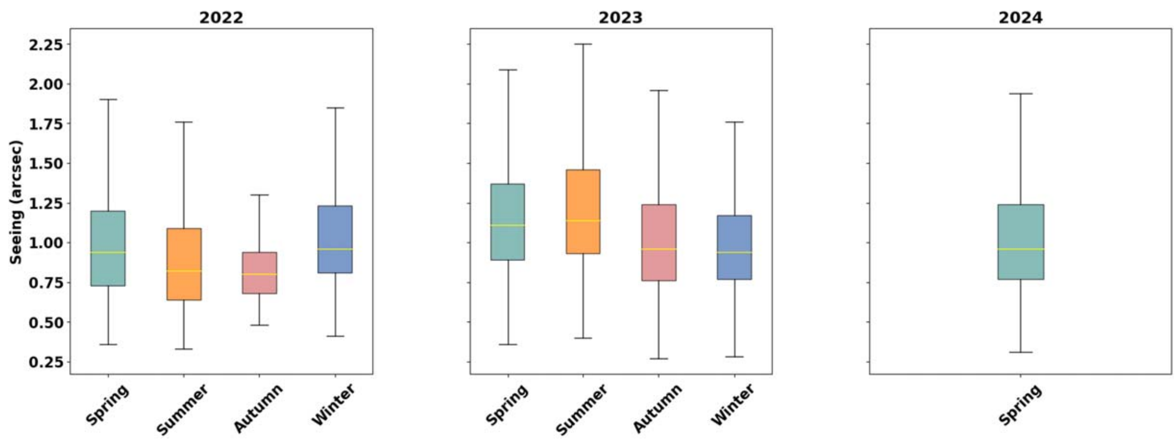

Figure 17. Seasonal box plots of seeing statistics for Platform C (2022–2024). Boxes signify the interquartile range, whiskers extend to the minimum and maximum values, and the yellow line represents the seeing median values.

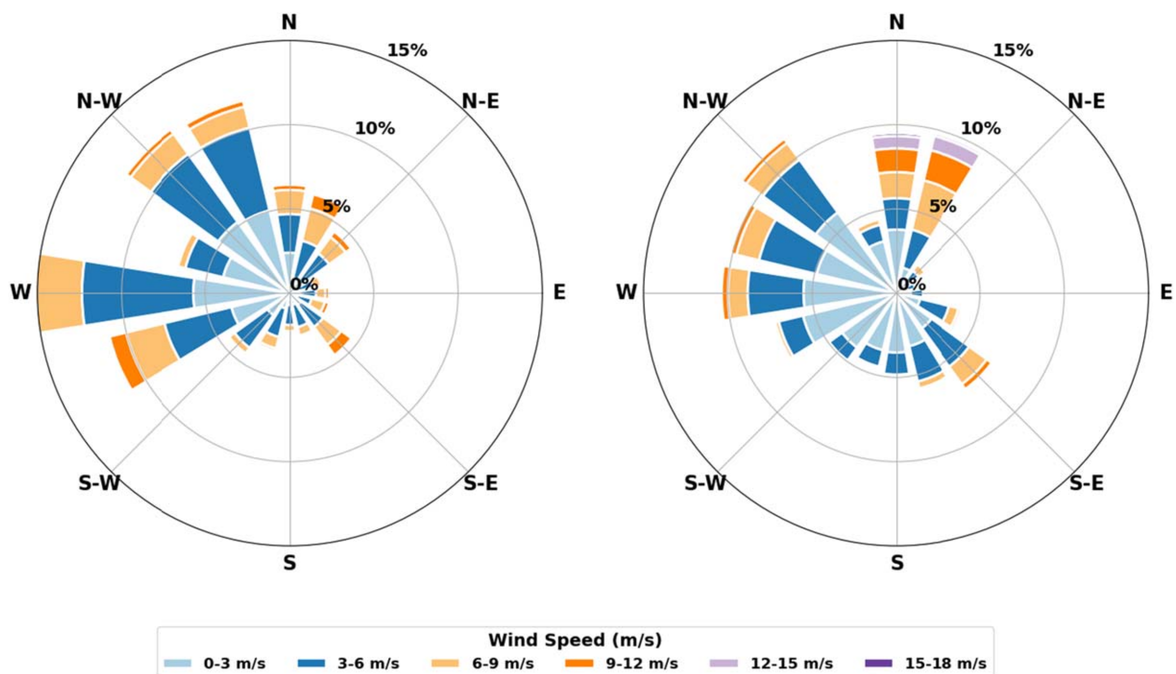

Figure 18. Wind rose diagrams for Platform A (left) and Platform C (right), covering the period from 2024 January to June.

Platform C after midnight. To explore this difference, we analyzed wind speed and wind direction data. Figure 14 shows minor differences between the two platforms, implying a limited impact of macro-scale wind properties on visual clarity differences. However, the higher frequency of west winds on Platform A compared to Platform C (in Figure 15) may suggest that Platform C is more sheltered by the surrounding buildings. Local microclimate effects, such as the heat released by buildings at night that increases local air instability and near-surface turbulence, may be responsible for the deterioration of seeing at Platform C after midnight. In contrast, Platform A, which is located in a more open environment, experiences less local thermal disturbance and thus maintains better seeing conditions.

5. Seasonal Characteristics

Figures 16 and 17 illustrate the wind roses and seeing statistics for different seasons from 2022 to 2024 for Platform

C. The results indicate that the best seeing value was observed in 2022, characterized by prevailing west or southwest winds in spring, summer, and fall, and northwest wind in winter. However, the west wind became more prevalent only in fall and winter, which may have improved seeing during these seasons. In spring 2024, the comparison between Platform A and Platform C (in Figure 18) shows that both platforms were mainly influenced by north winds. However, Platform A had a higher proportion of west and southwest winds, which may have contributed to slightly better seeing. Overall, wind direction significantly impacts seeing quality, with west or southwest winds associated with better conditions. Local variations in wind direction further underscore its critical role in determining seeing quality.

6. Conclusion

In this paper, we present a statistical analysis of the seeing conditions at the Lenghu site Platform C from 2018 to 2024. We also investigated the influence of key meteorological parameters, including wind speed, wind direction, and building-induced obstruction, on the quality of the seeing. The main conclusions are as follows:

(1) An analysis of 1,125,467 seeing records from the DIMM equipment revealed a progressive decline in seeing quality across different locations. The median seeing values were 0.″76 for C1, 0.″83 for C2, and 0.″99 for C3, indicating that changes in the observational environment, particularly those associated with location development, may impact seeing quality. It should be noted, however, that some of these measurements were taken at different times and locations. As a result, variations in local topography and natural atmospheric conditions could influence the data, and the absence of simultaneous multi-location measurements makes it challenging to pinpoint the precise causes of the observed degradation.

(2) Wind speed and wind direction affected seeing quality. Optimal seeing occurred with wind speeds of 2–6 $\mathrm{m\,s^{-1}}$ and directions between 180° and 270°. In 2023 and 2024, lower wind speeds, particularly during C3, correlated with a decline in seeing quality. Wind rose analysis showed a shift from southwest to northwest winds, with more north wind, altering local observational conditions.

(3) The construction of the WFST modified the local wind field at the surface layer, causing changes in wind direction, reduced wind speed and increased turbulence at the location of the DIMM. These factors degraded seeing quality for telescopes downwind of the WFST. CFD simulations indicated wind disturbances of 225°–255°, aligning with observed data. Analyzing seeing data from different WFST construction phases showed median values of 0.″79, 0.″88, and 0.″98, respectively. Comparisons with Platform A, located at a higher, more open environment, consistently showed better seeing, especially after midnight. This discrepancy is likely due to building-induced occlusion and nocturnal heat-driven turbulence.

(4) To improve seeing quality in future observatories, efforts should focus on optimizing the design and layout of both buildings and equipment to minimize disturbances in the local wind field. On 2024 April 27, the pillar supporting the telescope was raised to bring it closer to the free atmosphere, which slightly improved the statistical result of the seeing data. The actual seeing condition at Platform C is likely not deteriorating over time but is being modified by the buildings. To better measure the natural seeing conditions, a new location for the site quality monitoring system is recommended.

Acknowledgments

This work is mainly supported by the grant 2023FY101100 of the Ministry of Science and Technology of China (MOST) and the key project of the National Natural Science Foundation of China (NSFC, grant No. 12233009). The authors acknowledge the support from the National Natural Science Foundation of China (NSFC, grant Nos. 12273064, 42222408, 12322306, and 12373093).

ORCID iDs

Taoran Li https://orcid.org/0000-0003-1795-0742

References

Barker, E. S. 1987, Site testing with an acoustic sounder at McDonald Observatory: theory and practice, in Int. Conf. Identification, Optimization and Protection of Optical Telescope Sites (Flagstaff, AZ: IOPO Conf.), 49
Blocken, B., & Carmeliet, J. 2004, J. Thermal Envelope and Building Sci., 28, 107
Bely, P.-Y. 1987, PASP, 99, 560
Coulman, C. E. 1985, ARA&A, 23, 19
Deng, L., Yang, F., Chen, X., et al. 2021, Natur, 596, 353
Feng, L., Hao, J.-X., Cao, Z.-H., et al. 2020, RAA, 20, 080
Giovanelli, R., Darling, J., Sarazin, M., et al. 2001, PASP, 113, 789
Jabiri, A., Benkhaldoun, Z., Vernin, J., & Muñoz-Tuñón, C. 2000, A&AS, 147, 271
Li, T.-R., & Jiang, X.-J. 2022, RAA, 22, 045002
Liu, L. Y., Giordano, C., Yao, Y. Q., et al. 2015, MNRAS, 451, 3299
Munoz-Tunon, C., Vernin, J., & Varela, A. M. 1997, A&AS, 125, 183
Roddier, F. 1981, PrOpt, 19, 281
Sarazin, M., & Roddier, F. 1990, A&A, 227, 294
Tokovinin, A. 2023, Atmos, 14, 1694
Van Kooten, M. A. M., & Izett, J. G. 2022, PASP, 134, 095001
Woltjer, L. 1991, Msngr, 64, 5
Zhu, L., Zhang, H., Zhang, L., et al. 2023, MNRAS, 525, 3236